IOP Publishing J. Phys. Mater. 8 (2025) 035005 https://doi.org/10.1088/2515-7639/ade292

Journal of Physics: Materials

OPEN ACCESS

RECEIVED
6 March 2025

REVISED
28 May 2025

ACCEPTED FOR PUBLICATION
9 June 2025

PUBLISHED
19 June 2025

PAPER

Time-dependent dichroism and transient valley polarisation in monolayer transition metal dichalcogenides under finite-pulse radiation

Alejandro S Gómez[1,2], **Yuriko Baba**[1,2], **Francisco Domínguez-Adame**[2] and **Rafael A Molina**[3,*]

[1] Condensed Matter Physics Center (IFIMAC), Universidad Autónoma de Madrid, E-28049 Madrid, Spain
[2] GISC, Departamento de Física de Materiales, Universidad Complutense, E-28040 Madrid, Spain
[3] Instituto de Estructura de la Materia IEM-CSIC, Serrano 123, E-28006 Madrid, Spain
[*] Author to whom any correspondence should be addressed.

E-mail: rafael.molina@csic.es, alejandros.gomez@estudiante.uam.es and yuriko.baba@uam.es

Keywords: transition metal dichalcogenides, Floquet physics, time-dependent dichroism, finite pulses

Supplementary material for this article is available online

Abstract

Recent advances in time-resolved angle-resolved photoemission spectroscopy have enabled access to ultrafast electron states and their spin dynamics in solids. Atomically thin transition metal dichalcogenides are paradigmatic two-dimensional materials where electron momentum and spin degrees of freedom are coupled, being suitable candidates for time-resolved spectroscopy studies. In this work, we present a thorough study of the electron dynamics when these materials are subject to an intense finite-pulse driving radiation. We extend the scope of the conventional Floquet engineering and rely on the so-called $t-t'$ formalism to deal with driving fields described with two distinct time scales, namely the envelope amplitude timescale and the time period of the external field. The interplay between the finite-pulse timescales and the intrinsic properties of the electrons gives rise to transient valley polarisation and dynamical modifications of band structures, revealed by the time-dependent circular dichroism of the sample.

1. Introduction

Floquet engineering has emerged as a powerful tool for dynamically tailoring the properties of quantum materials by applying time-periodic perturbations [1, 2]. This approach has been widely explored for its ability to manipulate novel electronic and topological phases in systems ranging from ultracold atoms [3–5] to solid-state materials [6–8]. However, most theoretical treatments of Floquet phenomena rely on the assumption of perfectly periodic driving fields, which may not accurately reflect practical experimental settings as usually large amplitudes of the driving field are required and ultrashort laser pulses need to be used. In this context, time-resolved ARPES measurements have revealed the dynamics of Floquet–Bloch states at the surface of three-dimensional topological insulators [6, 7]. Remarkably, recent advances in the time resolution of ARPES measurements [9–12] make it possible to address the dynamics of topological states with subcycle precision [11]. Coherent control and observation of Floquet–Bloch states require that the time-scales of the dynamics of electrons coupled with the external field dominate over scattering mechanisms due to phonons and defect. This has been demonstrated experimentally in WTe_2 at room temperature [9]. However, in the same work Floquet replicas could not be observed experimentally in graphene. The theoretical analysis showed that this was probably due to competing time scales between the Floquet dynamics and the scattering events, highlighting the importance of strong fields and long scattering times in Floquet-engineering applications. The indirect measurements of Floquet topological properties as the anomalous Hall effect [8, 13] and the very recent observations of Floquet states by ARPES in graphene [14, 15] have been performed at lower temperatures and, thus, longer scattering times.

Two-dimensional materials are particularly well-suited for exploring the concepts of Floquet engineering, as the issue of light penetration depth is inherently negligible. Indeed the first theoretical proposals for

Floquet engineering of topological properties were made in 2D materials [18, 23]. However, experimental advances in Floquet engineering of 2D topological materials have been slow and difficult. Challenges such as heating and decoherence remain significant obstacles. In spite of all these problems, several key experimental results have demonstrated remarkable control over electronic and optical properties through periodic driving. For instance, anomalous Hall conductivity induced by light has been measured in graphene [8] although direct evidence of topological states is still lacking. Nevertheless, transport conductivity measurements could be used as a signature of light-induced band gaps in graphene as suggested in recent studies [16]. Additional evidence of Floquet band engineering includes the observation of gap opening due to avoided crossings of Floquet–Bloch bands in the surface of a topological insulator [6] as well as Floquet-induced band inversion in 2D phosphorene [24].

Atomically thin transition metal dichalcogenides (TMDs), with their rich electronic structures, strong spin–orbit coupling, and valley-selective optical response, offer a particularly intriguing platform for studying applications of Floquet engineering [17, 19–22]. Already, valley-selective excitations and coherent control of excitons have been achieved in TMDs using finite optical pulses, highlighting the potential for valleytronics applications [25, 26].

A very relevant development regarding coherent control of material properties by light is the use of tailored pulses with increasing possibilities of symmetry breaking control [27]. Theoretically investigated effects include the use of bichromatic pulses [28–31], twisted light [33], and periodic intensity modulation [32]. Experimentally, there has been some advances in 2D materials. For example, a light-wave-controlled Haldane model in monolayer hexagonal boron nitride was reported using a structured spatial waveform of the light field controlled with subcycle precision [34].

Additional theoretical efforts are required to address more realistic experimental conditions, such as the finite duration of laser pulses, which deviates from the idealised assumption of perfectly periodic driving. These temporal constraints can significantly affect the formation, stability, and observability of Floquet states, potentially altering their spectral properties and leading to non-trivial transient dynamics that must be carefully modelled to ensure accurate comparison with experimental results. There has been some important advances in describing subcycle time-dependent ARPES pump–probe spectroscopy with applications to graphene and hexagonal boron nitride [29, 32, 35]. Recent experiments measuring photocurrents in graphene illuminated by a circularly polarised femtosecond laser pulse have shown subcycle sensitivity [13].

In this work, we extend the scope of Floquet engineering applied to TMDs by considering finite-pulse driving schemes within the $t - t'$ formalism [36–41]. This formalism offers a natural framework to describe the temporal evolution of systems subjected to driving fields with arbitrary time profiles. It requires consideration of two distinct time scales: the envelope amplitude timescale and the time period of the external field. For the method to be effective, the period associated with the field frequency must be significantly shorter than the envelope timescale. In this way, the pulse driving is described using an instantaneous Floquet basis, with the pulse amplitude as a decoupled parameter. By applying this methodology to TMDs, we aim to elucidate how finite-pulse radiation influences the emergence of Floquet states, their spectral features, and the resulting valley dynamics.

Our analysis reveals that the interplay between the finite-pulse characteristics and the intrinsic properties of TMDs gives rise to distinctive effects, including transient valley polarisation and dynamical modifications of band structures that depend on the pulse shape and duration. We focus on the time-dependent circular dichroism (CD) as the experimental signature to detect these dynamical effects. These findings broaden the theoretical understanding of Floquet engineering applied to two-dimensional materials and offer experimentally relevant insights for designing optoelectronic devices and exploring ultra-fast valleytronics applications in TMDs.

2. Method

In monolayer TMDs such as MoS_2, $MoSe_2$, WS_2 and WSe_2 the conduction- and valence-band edges are located at valleys **K** and **K**′ of the hexagonal Brillouin zone [42, 43]. The conduction band exhibits a small spin splitting, which becomes more pronounced in heavier materials such as WTe_2. However, this splitting is typically negligible in most TMDs and therefore omitted in the following. In contrast, the valence band shows a large spin splitting due to the enhanced spin–orbit coupling, see a schematic plot in figure 1(a). By comparison with *ab-initio* calculations, it is shown that the electron states close to the band edges can be accurately described by the following two-band spinfull $\boldsymbol{k}\cdot\boldsymbol{p}$ Hamiltonian [44]

$$\mathcal{H}_0\left(k_x,k_y\right)=\hbar v\left(\tau k_x\hat{\sigma}_x+k_y\hat{\sigma}_y\right)+\frac{\Delta}{2}\hat{\sigma}_z-\lambda\tau\frac{\hat{\sigma}_z-\hat{\sigma}_0}{2}\hat{s}_z\,, \tag{1}$$

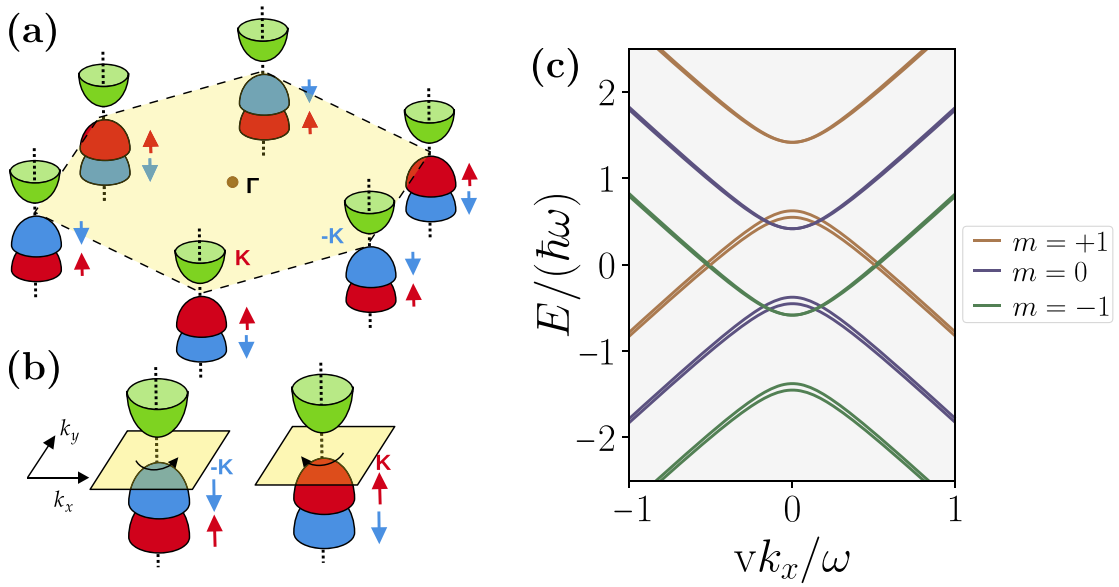

Figure 1. (a) Schematic representation of the MoS_2 band structure in the two-dimensional Brillouin zone close to the band edges. Valley's conduction bands (in green) are considered degenerated while valence bands (in red and blue) are split by the spin–orbit coupling (up/down arrows). (b) Enlarged view of the inequivalent valleys $\tau = -1$ (left) and $\tau = +1$ (right), highlighting their opposite chiralities. (c) Calculated band spectrum of MoS_2 including Floquet replicas $m = 0, +1, -1$. The driving frequency is set to $f = \omega/2\pi = 120$ THz, corresponding to a photon energy $\hbar\omega = 2$ eV.

where $\tau = \pm 1$ is the valley index. Here $\hat{\sigma}_j$ $(j = x, y, z)$ and $\hat{\sigma}_0$ denote the Pauli matrices and the 2×2 unit matrix acting upon the basis functions. Similarly, $\hat{s}_z$ and $\hat{s}_0$ are the Pauli matrix and the 2×2 unit matrix for spin. In equation (1), v is a model parameter with dimensions of velocity, Δ is the energy gap, and λ is the spin splitting at the valence-band edge. The dispersion relation is:

$$E_{c\uparrow(c\downarrow)} = \mathcal{M}_\tau \pm \frac{\lambda\tau}{2}, \quad E_{v\uparrow(v\downarrow)} = -\mathcal{M}_\tau \pm \frac{\lambda\tau}{2}, \tag{2}$$
$$\mathcal{M}_\tau\left(k_x, k_y\right) = \sqrt{(\hbar v)^2\left(k_x^2 + k_y^2\right) + \frac{1}{4}(\Delta \pm \lambda\tau)^2},$$

where the subscript c (v) refers to the conduction (valence) band and the $\uparrow$ $(\downarrow)$ to the spin up (down), which relates to the $+(-)$ sign.

The external pulse is included via the Peierls substitution $\hbar\mathbf{k} \to \hbar\mathbf{k} + e\boldsymbol{A}(t)$. The time-dependent Hamiltonian obtained is

$$\mathcal{H}\left(k_x, k_y, t\right) = \mathcal{H}_0\left(k_x, k_y\right) + V(t), \tag{3a}$$
$$V(t) = \frac{evA(t)}{\sqrt{1+\varepsilon^2}}\left[\tau\cos(\omega t + \varphi)\sigma_x + \varepsilon\sin(\omega t + \varphi)\sigma_y\right]s_0, \tag{3b}$$

where $\varepsilon = \tan(\chi)$ gives the ellipticity of the light, being $\varepsilon = +1$ for right-handed polarisation and $\varepsilon = -1$ for left-handed. ω is the frequency of the pulse, φ is the carrier-envelope phase (CEP), and the amplitude is given by a time-dependent function $A(t)$. Note that, due to the sign exchange between valleys the trajectory of $\hbar\boldsymbol{k} + e\boldsymbol{A}(t)$ around a Dirac point in a circularly polarised light field is opposite for the two valleys, see figure 1(b). For the sake of concreteness, we will employ a Gaussian-shape envelope, although any other differentiable function can be implemented within the method explained hereafter. Therefore

$$A(t) = A_0 e^{-(t/\gamma)^2}, \tag{4}$$

where A_0 is the maximum amplitude and $\gamma > 0$ has units of time and gives the width of the Gaussian pulse.

Even when the pulse is not strictly periodic, we can define a Floquet–Fourier expansion at a fixed amplitude by considering two time-scales and writing equation (3*b*) as:

$$V(t, t') = \frac{evA(t')}{\sqrt{1+\varepsilon^2}}\left[\tau\cos(\omega t + \varphi)\sigma_x + \varepsilon\sin(\omega t + \varphi)\sigma_y\right]s_0. \tag{5}$$

Notice that now the time-periodicity is restored for time t leading to $V(t,t') = V(t+T,t')$, where $T = 2\pi/\omega$ is the period of the internal oscillations of the pulse. The method of decoupling the envelope time-dependence from the frequency oscillation of the pulse is known as the $t-t'$ formalism, and it is employed to describe the time-evolution of the system in a Floquet-like basis for non-periodic pulses [36, 38–41]. For a fixed $A(t')$, the expansion over the Fourier harmonics is defined in the usual way

$$H_{mn}(t') = \frac{1}{T}\int_T \mathrm{d}t\left[\mathcal{H}_0\left(k_x,k_y\right) + V(t,t')\right]\mathrm{e}^{\mathrm{i}(m-n)\omega t} - m\hbar\omega\delta_{m,n}\,, \tag{6}$$

where m,n are integers corresponding to the *harmonic* indices of the Fourier expansion. The Floquet–Fourier Hamiltonian is then obtained by writing the former equation in a matrix form as

$$H_{\mathrm{F}}(\mathbf{k},A(t')) = \begin{pmatrix} \ddots & Q(A(t')) & 0 & & \\ Q^{\dagger}(A(t')) & H_0(\mathbf{k})+\hbar\omega & Q(A(t')) & 0 & \\ 0 & Q^{\dagger}(A(t')) & H_0(\mathbf{k}) & Q(A(t')) & 0 \\ & 0 & Q^{\dagger}(A(t')) & H_0(\mathbf{k})-\hbar\omega & Q(A(t')) \\ & & 0 & Q^{\dagger}(A(t')) & \ddots \end{pmatrix}, \tag{7}$$

where the term that couples the Fourier replicas is the one of a monochromatic field and it is given as

$$Q(A(t')) = \frac{ev}{2\sqrt{1+\varepsilon^2}}A(t')\left(\tau\sigma_x+\varepsilon\sigma_y\right)s_0\mathrm{e}^{-\mathrm{i}\varphi}\,. \tag{8}$$

The solution of the eigenvalue problem for H_{F} (7) for a fixed $A(t')$ gives the Floquet quasi-energies $\xi_b^{(m)}(\mathbf{k},A)$ and the Fourier modes $|u_b^{(m)}(\mathbf{k},A)\rangle$, with $b = \{c_\uparrow, c_\downarrow, v_\uparrow, v_\downarrow\}$ denoting the four bands of the model and m the Fourier component. The quasi-energies and the Floquet–Fourier modes define the so-called instantaneous Floquet basis

$$|\phi_b^F(\mathbf{k},t)\rangle = \mathrm{e}^{-\mathrm{i}\xi_b(\mathbf{k},A)t/\hbar}\,|u_b(\mathbf{k},A,t)\rangle\,, \tag{9}$$

where the amplitude $A = A(t')$, the quasienergy is fixed by $\lim_{A\to 0}\xi_b(\mathbf{k},A) \to E_b(\mathbf{k})$, and

$$|u_b(\mathbf{k},A,t)\rangle = \sum_{m=-\infty}^{\infty}\mathrm{e}^{-\mathrm{i}m\omega t}\,|u_b^{(m)}(\mathbf{k},A)\rangle\,. \tag{10}$$

The Fourier components $u_b^{(m)}$ in (10) can be used to define the time-averaged spectral function $\overline{\rho}(\mathbf{k},E)$. For a fixed amplitude A, i.e. for a perfectly periodic Floquet system, this quantity is given by

$$\overline{\rho}(\mathbf{k},E) = \sum_{\alpha}\langle u_b^{(m)}(\mathbf{k})|u_b^{(m)}(\mathbf{k})\rangle\delta\left(\xi_b + m\hbar\omega - E\right)\,. \tag{11}$$

The time-averaged spectral function for MoS_2 is represented in figure 2(a) in the limit of a small amplitude pulse. For later use, it is convenient to define the double index $\alpha \equiv (b,l)$ that labels the band b and the replica l, and the following quantities

$$\xi_\alpha(\mathbf{k},A) \equiv \xi_b(\mathbf{k},A) + l\hbar\omega\,, \tag{12a}$$

$$|u_\alpha(\mathbf{k},A,t)\rangle \equiv \mathrm{e}^{\mathrm{i}l\omega t}|u_b(\mathbf{k},A,t)\rangle\,. \tag{12b}$$

An example of the replicas appearing in the Floquet spectra is shown in panel 1(c), where the two replicas with $m = \pm 1$ are represented for a fixed amplitude.

The $t-t'$ formalism consists in mapping the time-evolution of the time-dependent Schrödinger equation (TDSE) for the full Hamiltonian (3*a*) given by

$$\mathrm{i}\hbar\frac{\mathrm{d}}{\mathrm{d}t}|\psi(\mathbf{k},t)\rangle = \mathcal{H}(\mathbf{k},t)\,|\psi(\mathbf{k},t)\rangle\,, \tag{13}$$

to the instantaneous Floquet basis by writing the solution as:

$$|\psi(\mathbf{k},t)\rangle = \sum_{\alpha}C_\alpha(\mathbf{k},t)\,|u_\alpha(\mathbf{k},A(t),t)\rangle\,, \tag{14}$$

where the coefficients C_α satisfy

$$\mathrm{i}\hbar \frac{\mathrm{d}C_\alpha(\mathbf{k},t)}{\mathrm{d}t} = \sum_\beta \mathcal{H}^{tt'}_{\alpha\beta}(\mathbf{k},A(t))\, C_\beta(\mathbf{k},t)\ , \tag{15}$$

with

$$\mathcal{H}^{tt'}_{\alpha\beta}(\mathbf{k},A(t)) \equiv \delta_{\alpha\beta}\xi_\alpha(\mathbf{k},A(t)) - \mathrm{i}\hbar \frac{\mathrm{d}A}{\mathrm{d}t}\mathcal{G}^{tt'}_{\alpha\beta}(\mathbf{k},A(t))\ , \tag{16a}$$

$$\mathcal{G}^{tt'}_{\alpha\beta}(\mathbf{k},A(t)) \equiv \frac{1}{T}\int_T \mathrm{d}t' \langle u_\alpha(\mathbf{k},A(t),t')\,|\partial_A|u_\beta(\mathbf{k},A(t),t')\rangle\ . \tag{16b}$$

Here, $\partial_A = \partial/\partial A$. The instantaneous Floquet states in (16*b*) are assumed to be differentiable, and we chose the gauge of the parallel transport over the states by setting $\langle u_\alpha(A,t)|\partial_A|u_\alpha(A,t)\rangle = 0$. It is important to note that, being equivalent to the solution of the TDSE, the $t-t'$ formalism extends beyond the Floquet adiabatic approximation. However, it fails to accurately capture the system's dynamics when the instantaneous Floquet basis cannot be consistently defined within the parallel transport gauge. This limitation arises in systems where spectral degeneracies cannot be factorized consistently across all amplitude regimes. More details about the implementation of the $t-t'$ formalism can be found in [41].

Finally, to relate the calculated coefficients to an observable quantity, we define the integrated power over time of the $C_\alpha(\mathbf{k},t)$ coefficients as

$$P(\Omega) = \int \mathrm{d}\mathbf{k} \int \mathrm{d}t \sum_\alpha |C_\alpha(\mathbf{k},t)|^2 L(\Omega,\varepsilon_\alpha,\Gamma)\ , \tag{17}$$

where we are integrating in a time-window such that the amplitude $A > A_{\min}$, with $A_{\min}$ being a numerical cutoff. In the previous expression $L(z,z_0,\Gamma)$ is the Lorentzian function defined as:

$$L(z,z_0,\Gamma) = \frac{1}{\pi}\frac{\Gamma}{(z-z_0)^2+\Gamma^2}\ . \tag{18}$$

As a reference of the initial state, we define the limit of $P(\Omega)$ integrated for $A_0 \to 0$ or, equivalently, fixing the limit of $\delta(t-t_0)$ and employing (14). In this limit, we obtain

$$\begin{aligned} P_0(\Omega) &= \int \mathrm{d}\mathbf{k} \int \mathrm{d}t \sum_\alpha |C_\alpha(\mathbf{k},t)|^2 L(\Omega,\varepsilon_\alpha,\Gamma)\,\delta(t-t_0) \\ &= \sum_\alpha \int \mathrm{d}\mathbf{k} |\langle u_\alpha(\mathbf{k})|\psi(\mathbf{k},t=t_0)\rangle|^2 L(\Omega,\varepsilon_\alpha,\Gamma)\ . \end{aligned} \tag{19}$$

The quantity $P_0(\Omega)$ concerns the initial distribution of replica weights given an initial state ψ_0 and it can be employed as a comparison with $P(\Omega)$, which accounts for the weights after the pulse has been applied to the system.

Finally, to quantify the effect of the pulse polarisation, we analyse the CD of this integrated power [45, 46]:

$$\mathrm{CD}(\Omega) = \frac{|P^{\circlearrowright}| - |P^{\circlearrowleft}|}{|P^{\circlearrowright}| + |P^{\circlearrowleft}|}\ , \tag{20}$$

where the superscript stands for light polarisation, being $\varepsilon = +1$ the right-handed ($\circlearrowright$) and $\varepsilon = -1$ the left-handed ($\circlearrowleft$) light polarisation.

In this work, and for all subsequent numerical simulations, we consider molybdenum disulphide (MoS_2) as the material platform. The adopted parameters are: Fermi velocity $\hbar v = 3.512\,\mathrm{eV\AA}$, bandgap $\Delta = 1.66\,\mathrm{eV}$, and spin–orbit coupling $\lambda = 0.15\,\mathrm{eV}$ [47]. The driving frequency is set to $f = \omega/2\pi = 240\,\mathrm{THz}$, corresponding to a photon energy $\hbar\omega = 1\,\mathrm{eV}$. If not stated otherwise for the integrated power $P(\Omega)$ the cut-off amplitude employed is $A_{\min}/(\hbar\omega) = 0.01$. We employ a maximum pulse amplitude $A_{\max}$ ranging from 0.7 to 1 $\hbar\omega$. These amplitudes correspond to peak electric fields $E_{\max}$ between 2 to $2.8\,\mathrm{V\,nm^{-1}}$, and peak intensities $I_{\max}$ in the range $(5.3\text{–}10)\times 10^{11}\,\mathrm{W\,cm^{-2}}$.

We have not taken into account phonon and other decoherence effects in our model. As mentioned in the Introduction, the observation of Floquet sidebands require that dephasing mechanisms be slower than the electron-field dynamics. Through weak localisation measurements, a phase coherence time of 0.8 to 2 ps was reported in bilayer MoS_2 [48] while the electronic dynamics at strong fields is much faster, of the order of fs.

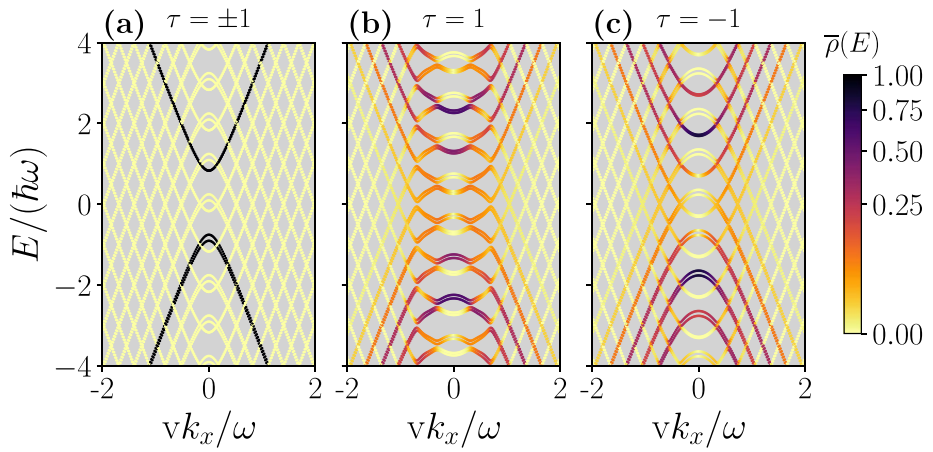

Figure 2. Floquet spectrum for a fixed pulse amplitude $A_x = A_y = 0$ in panel (a) and $A_x = A_y = 2.5v/\omega$ in panels (b) and (c). The valleys are indicated on top of the figure, both inequivalent valleys $\tau = \pm 1$ are considered. The colour code corresponds to the time averaged DOS $\overline{\rho}(E)$ computed according to (11). The pulse polarisation is set to a right-handed circular polarisation, i.e. setting $\varepsilon = +1$ in (3*b*). The spectra are plotted for $k_y = 0$.

3. Results and discussion

First, we briefly analyse the effect of the circularly polarised pulse on the valleys in the case of a constant amplitude. To show the distinct behaviour of $\tau = \pm 1$ valleys, we fix the external pulse to a right-handed circularly polarised monochromatic field, i.e. setting $\varepsilon = 0$ in (3*b*). The results for MoS_2 are shown in figure 2, where the time-averaged density of states $\overline{\rho}(E)$ from (11) is computed for a fixed amplitude A. The dichroism is visible in the distinct spectral features between the **K** ($\tau = +1$) and **K'** ($\tau = -1$) valleys, as evidenced by the contrast in the bandgap magnitudes appearing between Floquet replicas in figures 2(a) and (b). Specifically, the valley with chirality aligned to the pulse's handedness, in this case $\tau = +1$, exhibits significantly larger pulse-induced gaps. For the other valley, the spectral population is displaced to the replicas, but the Floquet quasienergies are not dramatically modified by the pulse, compare panel 2(b) with the spectrum for $A = 0$ in panel 1(c). However, even if the gaps in the $\tau = -1$ are almost negligible, it is important to stress that, due to the form of the time-dependent perturbation, $V(t)$ and the unperturbed Hamiltonian $\mathcal{H}_0$ do not commute and hence all band crossings between replica bands are avoided. The commutator is in fact given by

$$[\mathcal{H}_0, V(t)] = \mathrm{i}\frac{ev}{\sqrt{1+\varepsilon^2}} A(t) \Big\{ 2\hbar v\tau \left[k_x\varepsilon \sin(\omega t+\varphi) - k_y \cos(\omega t+\varphi)\right] \hat{\sigma}_z \otimes \hat{s}_0 + \left[\tau \cos(\omega t+\varphi)\,\hat{\sigma}_y - \varepsilon \sin(\omega t+\varphi)\,\hat{\sigma}_x\right] \otimes \left[\Delta \hat{s}_0 - \lambda\tau \hat{s}_z\right] \Big\}, \tag{21}$$

and hence it is generally non zero.

Next, we consider a finite pulse with Gaussian envelope given by (4). Within the $t - t'$ formalism, the time-dependent Floquet spectra are computed in figures 3 and 4 for the two valleys $\tau = \pm 1$ and fixed right-handed circular polarisation, i.e. $\varepsilon = +1$ in (3*b*). The time-dependent Floquet spectrum at time t resembles the corresponding time-periodic Floquet spectrum for constant amplitude $A(t)$. Therefore, the gapped structure between replicas is indeed enhanced only for the valley $\tau = +1$ in figure 3. For $\tau = -1$ the bands are displaced and renormalised by the pulse even if the gaps between replica bands are almost negligible, see figure 4. The figures include in colour code the expansion coefficients $C_\alpha(\mathbf{k}, t)$ for some selected times. Since $|C_\alpha(\mathbf{k}, t)|^2$ is related to the occupation of the Floquet replicas, it can be seen that the valley in which the chirality matches the polarisation of the pulse, in this case $\tau = +1$, the distributions of $C_\alpha(\mathbf{k}, t)$ coefficients achieve higher replica bands. Thus, the effect of the pulse when polarised in the valley direction is enhanced not only at the level of the appearance of gaps in the spectrum, but also in terms of populating higher replica states. The additional figures S4 and S5 in the supplemental material show additional time snapshots for completeness. The code for the calculations is available in the repository [49].

So far, we have discussed the impact of a fixed pulse on the two inequivalent valleys. However, a more convenient way of exploiting the effect of the external perturbation is to vary the external pulse itself so that the dynamics of the states can be tuned at will. In the case of the Gaussian pulse considered, the three parameters that can be modified are the Gaussian width γ, the CEP φ and the ellipticity angle χ. From equations (3*b*) and (1), it can be seen that the Hamiltonian (3*a*) is invariant under the following transformation

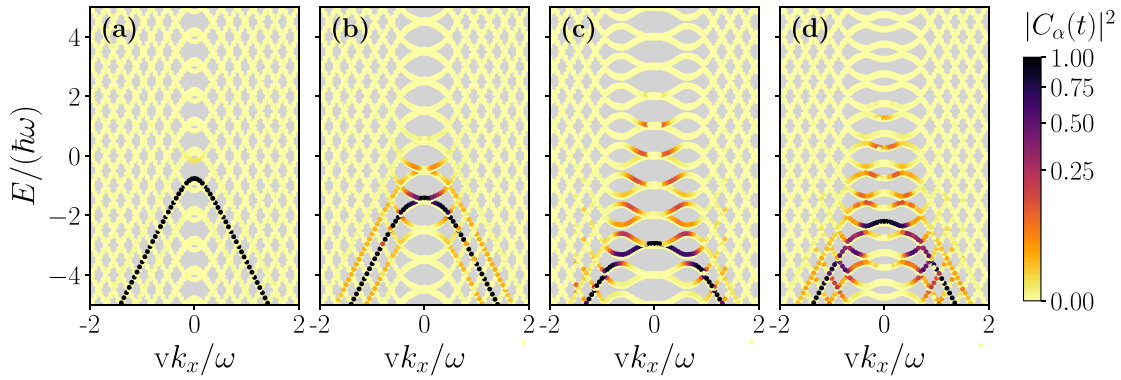

Figure 3. Time-dependent Floquet spectra for the valley $\tau = +1$ under a finite-pulse with right-handed circular polarisation ($\varepsilon = +1$) and Gaussian envelope centred at $t_0 = 0$ with a width $\gamma = T$, where T is the pulse period. The spectra are shown for $t/T = \{-2, -1, 0, 0.6\}$ in panels (a), (b), (c) and (d), respectively. We consider as initial state a fully occupied valence band with spin up $|v^0_\uparrow\rangle$ and a maximum amplitude $A_0 v/\omega = 3.5$. The colour code corresponds to $|C_\alpha(\mathbf{k}, t)|^2$.

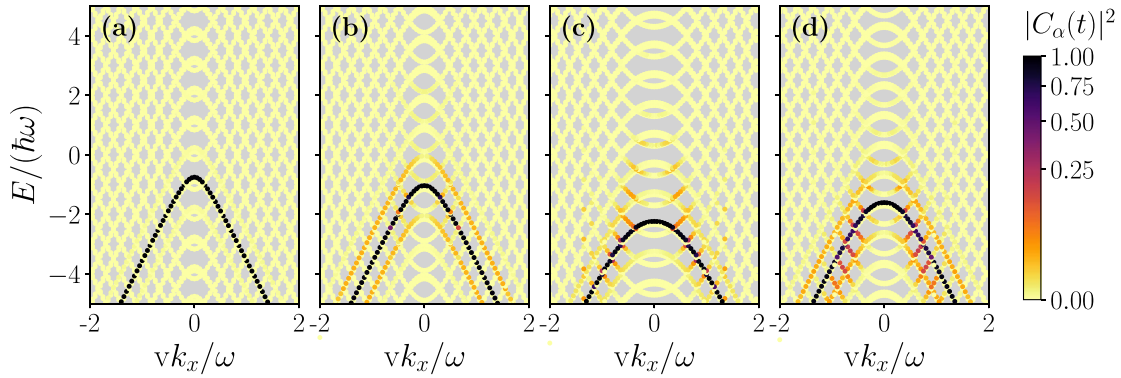

Figure 4. Same magnitudes as in figure 3 for the valley $\tau = -1$ considering as initial state $|\psi_0\rangle = |v^0_\downarrow\rangle$. The rest of the parameters are the same as in figure 3.

$$\tau \to -\tau\,, \quad \chi \to -\chi\,, \quad k_x \to -k_x \quad s_z \to -s_z\,.$$

Thus, the exchange of the valley index is equivalent to inverting the pulse polarisation, as well as the momentum k_x and the spin of the state. For this reason, in the following, we discuss the influence of the pulse parameters for a fixed valley polarisation $\tau = +1$, recalling that the results are equivalent for $\tau = -1$ upon the transformation above mentioned.

The evolution within the $t - t'$ formalism of a single (k_x, k_y) mode at fixed valley $\tau = +1$ is shown in figure 5 for different values of the width of the Gaussian envelope γ, corresponding to the columns of the figure. The initial state considered is $\psi_0 = |v^0_\uparrow\rangle$, corresponding to the spin-up valence state of the unperturbed Hamiltonian. The time-dependent Floquet quasi-energies are shown in panels 5(a)–(c), the squared probability amplitudes of the expansion coefficients $C_{(b,l)}$ in panels 5(d)–(f), and a comparison between the time evolution obtained via the $t - t'$ formalism and the direct integration of the TDSE is plotted in 5(g)–(i). The widths of the pulse are $\gamma/T = \{0.5, 1.0, 1.5\}$. For each pulse width γ, we observe the same qualitative evolution of the band populations, with the overall duration of these dynamics increasing as γ becomes larger, compare panels 5(d)–(f). The finite pulse does not mix spin states, and the distribution of Floquet replicas causes the system to alternate between conduction and valence states. Furthermore, as shown in figure 5, the width of the pulse also modifies the final state, while the specific Floquet replicas involved remain fixed by the maximum amplitude A_0 and the frequency ω, which determine the structure of the Floquet couplings and are unchanged for the three cases considered.

The comparison of the three pulse lengths in figure 5 is a clear example of the advantage of employing the $t - t'$ formalism to describe the dynamics of Hamiltonians with an underlying Floquet-like structure. In fact, by employing the Floquet picture, the system's evolution can be understood as a superposition of states with energies $E = \xi_b + m\hbar\omega$ which are populated according to the evolution of the Gaussian envelope. By analysing panels 5(d)–(f) we can distinguish mainly two regimes in the evolution as a function of time:

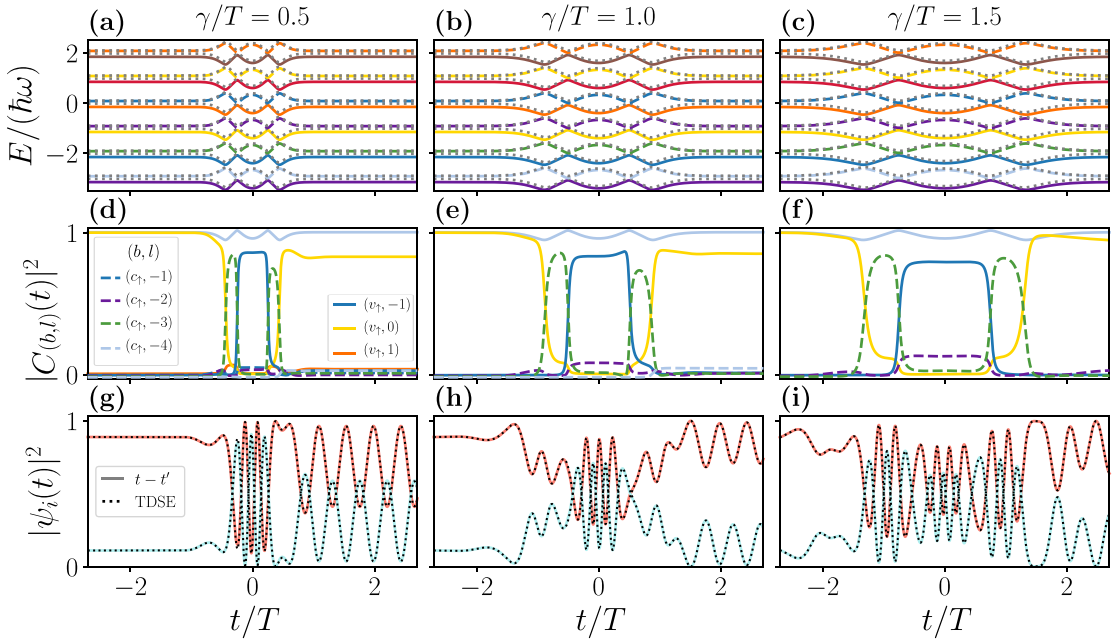

Figure 5. For $\tau = +1$ and right-handed polarisation we evaluate the time evolution of a single $\mathrm{v}/\omega(k_x, k_y) = (0.2, 0)$ mode, initialised in the state $|v^0_\uparrow\rangle$ of the unperturbed Hamiltonian. The width of the pulse is varied as $\gamma/T = \{0.5, 1.0, 1.5\}$. Panels (a), (b) and (c) show the Floquet spectra; panels (d), (e) and (f) display the squared probability amplitudes of the coefficients $C_{(b,l)}$; and panels (g), (h) and (i) compare the time evolution derived from the $t - t'$ formalism to that obtained from the direct integration of TDSE, expressed in the orbital basis. The maximum amplitude is set to $A_0 v/\omega = 2.5$.

- the adiabatic phase acquisition within the same Floquet replica given by the diagonal term. The adiabatic phase acquisition corresponds to the plateaus regions in the $|C_{(b,l)}|$ coefficients as a function of time, since the adiabatic phase acquisition is not visible in the absolute value of the expansion coefficients:
- the non-adiabatic transition between replicas, which correspond to the fast transitions between different $|C_{(b,l)}|$ coefficients. This second scenario is obtained in correspondence with avoided crossings of the time-dependent Floquet quasienergies, see panels 5(a)–(c). Formally, in the $t - t'$ formalism, the non-adiabatic transitions are obtained when the term $\mathcal{G}^{tt'}_{\alpha\beta}(\mathbf{k}, A(t))$ leads the time-evolution in (15).

Hence, increasing the pulse amplitude broadens these plateaus, reflecting the extended time during which the system stays in a given Floquet-like state. Finally, it is important to stress that the evolution in the $t - t'$ formalism is indeed equivalent to the solution of the TDSE, as it can be seen by the comparison of the lower panels of figure 5. In the $\psi(t)$ expressed in the orbital bases, the interference generated by the pulse can be seen in the oscillatory pattern as a function of t, which clearly shows distinct frequency regions. These distinct frequency regions correspond to the plateaus in panels (d)–(f), so that the change in the oscillation pattern of $\psi(t)$ in panels (g)–(f) can be explained by the time-dependent Floquet evolution of the expansion coefficients $C_{(b,l)}$.

Examining the dependence on the CEP φ provides additional insight into the preceding discussion, specifically by elucidating the different regimes delineated within the $t - t'$ framework. To understand this dependence, we first note that equation (8) shows that φ enters the coupling only through an overall factor $\exp(-\mathrm{i}\varphi)$ that multiplies the coupling term Q between first-neighbours Fourier replicas. For a time-independent amplitude this phase can be removed by a gauge transformation, so that the static Floquet quasienergies ξ_α are indeed independent of the CEP.

In the $t - t'$ formalism, the envelope $A(t)$ changes with time and the gauge cannot be chosen simultaneously at all instants, so the CEP reappears in the non-adiabatic term $\mathcal{G}^{tt'}_{\alpha\beta}$ in equation (16*b*). The CEP phase does not affect the Floquet quasi-energies ξ_α, since the spectra of (7) is independent of the hopping phase between Floquet replicas. However, the CEP does affect the time evolution of the expansion coefficients C_α via a phase acquisition. This accumulated phase is not visible in the absolute values of $|C_\alpha|$, but it is indeed obtained within the $t - t'$ formalism and it affects the time-dependent occupation of the orbitals, as shown in figure 6. In this sense, the CEP is a clear example of how the $t - t'$ formalism separates the contributions to the time evolution: the *adiabatic* phase acquisition due to the time-independent Hamiltonian given by the diagonal term in equation (16*a*), the CEP phase acquisition related to the non-adiabatic term $\mathcal{G}^{tt'}_{\alpha\beta}$ in equation (16*b*) and the magnitude of the expansion coefficient $|C_\alpha|$ that can be

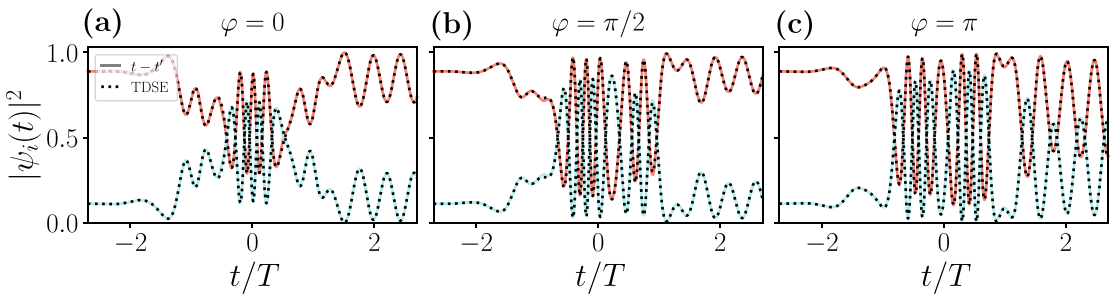

Figure 6. Time evolution of a single $v/\omega(k_x, k_y) = (0.2, 0)$ mode, initialised in the state $|v^0_\uparrow\rangle$ of the unperturbed Hamiltonian. We show the CEP φ dependence for $\varphi = \{0, \pi/2, \pi\}$ in (a)–(c), respectively. The maximum amplitude is set to $A_0 v/\omega = 2.5$. The width of the pulse is fixed to $\gamma/T = 1.0$, $\tau = +1$ and right-handed polarisation is considered. .

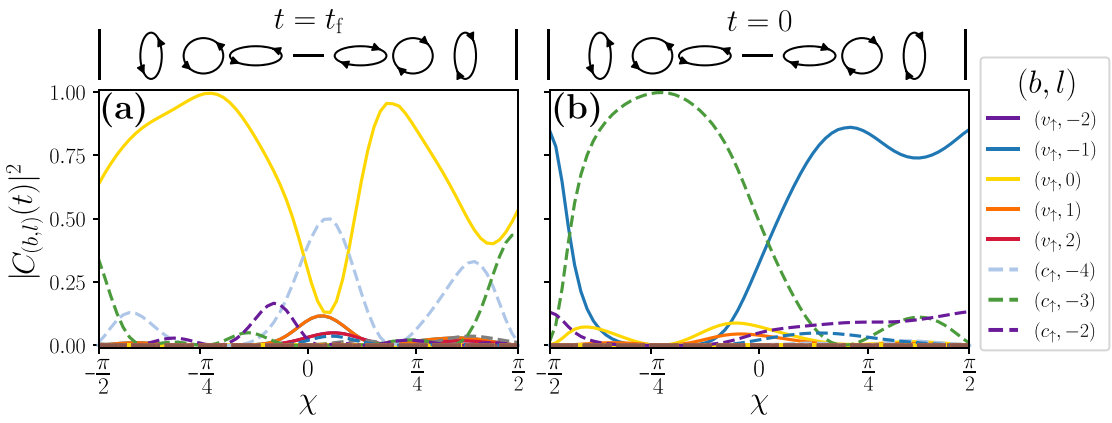

Figure 7. Squared amplitudes of the non-zero conduction and valence band coefficients $|C_{(b,l)}(t)|^2$ as a function of the ellipticity angle χ for a single mode $v/\omega(k_x, k_y) = (0.2, 0)$, at $\tau = +1$ valley and initialised state of $|v^0_\uparrow\rangle$. Panel (a) shows the final-state amplitudes at $t = t_f$. Panel (b) shows the amplitudes at the Gaussian peak time $t = 0$. The pulse width is fixed at $\gamma = 1$ and maximum amplitude $A_0 v/\omega = 2.5$.

interpreted as an occupation of the Floquet replicas. A more detail analysis of the phase evolution is included in the supplemental material S3.

In figure 7 we analyse the dependence on the ellipticity angle. For the sake of concreteness, we show the results for the same (k_x, k_y) mode described earlier, this time fixing the pulse width to $\gamma = 1$ and varying the ellipticity angle χ. In panel 7(a), we plot the final-state expansion coefficients $|C_{(b,l)}(t_f)|^2$ for a state initialised in $|v^0_\uparrow\rangle$ of the unperturbed Hamiltonian. In the limiting case of $\chi = -\pi/4$ (left-handed polarisation), the state returns to the initial state, consistently with the left-handed polarisation not matching the chirality of the $\tau = +1$ valley and hence not hybridizing the Floquet replicas. In the case of the right-handed polarisation, i.e. for $\chi = \pi/4$, the state is driven back to the initial valence state with high, but not unit, probability. Part of the occupation is indeed displaced to the conduction replica $(c_\uparrow, -4)$. This result is consistent with the right-handed polarisation matching the chirality of the $\tau = +1$ valley and hence generating a stronger coupling between replicas and wider gaps between conduction and valence sidebands. Interestingly, as χ deviates from these limiting left and right-handed cases, the transition to this lower conduction-band replica (without spin flipping) is increased, demonstrating the capability to select particular final states simply by adjusting the ellipticity angle.

We note that the driving field itself is symmetric under the exchange of the ellipse's long and short axes $\chi \to \pi/2 - \chi$. For modes that share the same on-plane symmetry $(k_x = k_y)$ this implies $|C_{(b,l)}(\chi)|^2 = |C_{(b,l)}(\pi/2 - \chi)|^2$. The mode used in figure 7 is $(k_x, k_y) = (0.2, 0)\omega/v$ and hence breaks that symmetry, so the obtained occupations are asymmetric around $\chi = \pi/4$. For a mode with equal $k_x = k_y$ the symmetry is restored, as shown in the supplemental material S6.

In figure 7(b) we show the same squared amplitudes at the time of maximum pulse amplitude, $t = 0$, corresponding to the peak of the Gaussian envelope. Here, the effect of the light's chirality on the final state becomes more pronounced. When the ellipticity angle χ matches the valley chirality $\varepsilon = 0$, the system is driven to an excited valence state. Conversely, for the opposite polarisation, a conduction state is induced,

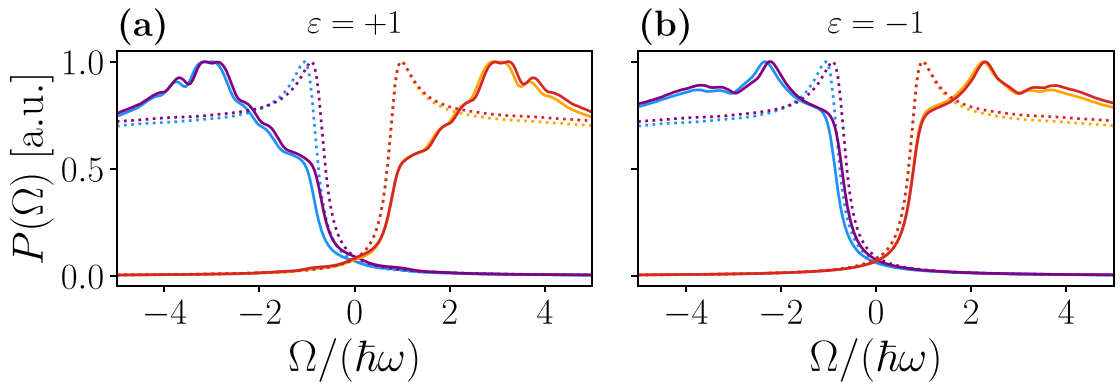

Figure 8. Integrated power $P(\Omega)$ for a fixed valley $\tau = +1$ and pulse amplitude $A_0 v/\omega = 2.5$. The dotted line $P_0(\Omega)$ indicates the initial distribution of replicas before applying the pulse. Panels (a) and (b) compare different initial states for right-handed ($\varepsilon = +1$) and left-handed ($\varepsilon = -1$) circular polarisation, respectively.

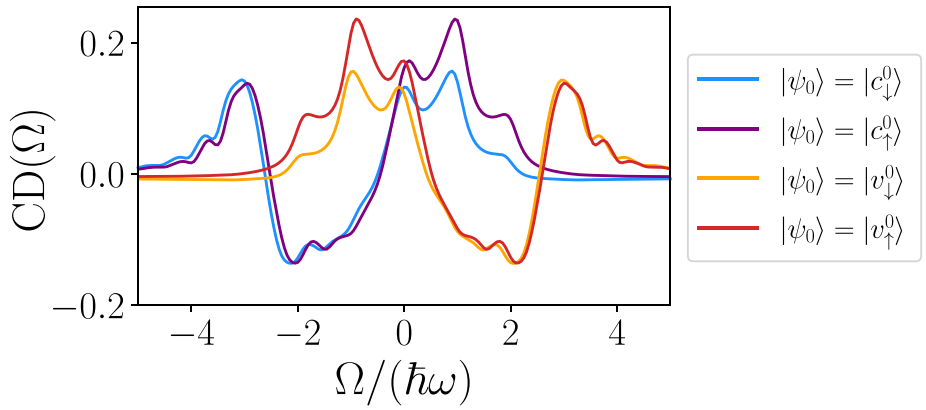

Figure 9. Circular dichroism CD(Ω) according to equation (20) for $\tau = +1$ and $A_0 v/\omega = 2.5$. Each curve corresponds to a different initial state indicated in the legend.

once again illustrating the ability to control and select the evolution of the states and the transitions between sidebands via the ellipticity angle of the incident light.

To gain insight into the distribution for all **k**-modes, we evaluate $P(\Omega)$, defined in equation (17), by integrating over all k_x momenta and times. We consider a fixed valley $\tau = +1$ and a pulse amplitude $A/(\hbar\omega) = 0.7$. The dotted curve $P_0(\Omega)$ indicates, as a reference, the initial distribution before the pulse is applied. In figure 8(a), we present the integrated power for several initial states when the polarisation of the pulse matches the chirality of the chosen valley. In addition, in figure 8(b), the polarisation is opposite to the valley chirality. When the polarisation and valley chirality coincide, figure 8(a), $P(\Omega)$ displays broader distributions in higher-energy (Floquet) replicas, indicating that higher sidebands are excited, along with a noticeable finer structure created by the wider gaps arising between sidebands. Conversely, for opposite chirality and polarisation, in figure 8(b), the system does not populate higher replicas so effectively and the structure of the peaks is broader, indicating that the gaps between sidebands are almost zero.

Finally, the CD is computed in figure 9 using (20) for the valley $\tau = +1$. Due to symmetry, an equivalent result holds for the other valley upon reversing the circular polarisation direction. We observe several pronounced peaks in CD(Ω) that are a signal of the difference in the structure of the gaps between replicas and the population of (and transitions to) higher-energy states under right-handed versus left-handed circular polarisation. The sign of the peaks indicates which polarisation is more strongly coupled as a function of the energy, reflecting the selective excitation of states with matching valley chirality. Thus, the appearance and magnitude of these CD peaks highlight how polarisation control can be leveraged to manipulate valley-selective processes and tune the occupation of higher Floquet sidebands even if finite-short pulses are employed.

4. Conclusions

In this work we have studied the effect of short pulses of radiation on single-layer TMDs. In particular, we examine pulses that can be described by two well-separated time-scales, one corresponding to the envelope of the amplitude and another related to the fast oscillations, which we consider of a fixed frequency ω. Employing the two time-scales, a time-dependent Floquet theory, called Floquet $t-t'$, can be formulated such that the Floquet states for each time-dependent amplitude value are employed as a basis to solve the time evolution of a given initial state. Within this formalism, the dynamics of the states can be interpreted in a time-dependent Floquet expansion, such that the evolution can be divided into two main regimes: the adiabatic acquisition of a phase and the non-adiabatic transition between Floquet sidebands. For the pulse amplitudes considered here, we find that the Floquet $t-t'$ formalism can be successfully employed even for pulses with few oscillations within the envelope function.

Regarding the results for the TMDs under circularly polarised irradiation, we have shown that the ellipticity angle χ can be employed to manipulate valley-selective processes related to the occupation of Floquet sidebands. In fact, if the polarisation matches the valley handedness, the Floquet sidebands are strongly coupled and quantities such as the integrated power $P(\Omega)$ or the $\mathrm{CD}(\Omega)$ show a structured peak shape as a function of the energy, corresponding to the induced gaps between sidebands, as well as the displacement of the population from the initial state to the higher Floquet replicas. In this way, the external pulse parameters, such as the pulse width or the ellipticity angle, can be employed to obtain valley-selective dynamics of the states and to probe the dichroic nature of these materials.

Data availability statement

The data that support the findings of this study are openly available at the following URL/DOI: https://github.com/yurikobd/Floquet_TMD_ttp.

Acknowledgments

We thank Klaus Richter for inspiring conversations. The work has been supported by Comunidad de Madrid (Recovery, Transformation and Resilience Plan), NextGenerationEU from the European Union (Grant MAD2D-CM-UCM5) and 'Talento Program' (Grant 2019-T1/IND-14088), Agencia Estatal de Investigación (Grant PID2022-136285NB-C31).

ORCID iDs

Alejandro S Gómez https://orcid.org/0009-0001-1117-4490
Yuriko Baba https://orcid.org/0000-0003-0647-3477
Francisco Domínguez-Adame https://orcid.org/0000-0002-5256-4196
Rafael A Molina https://orcid.org/0000-0001-5728-0734

References

[1] Aoki H, Tsuji N, Eckstein M, Kollar M, Oka T and Werner P 2014 *Rev. Mod. Phys.* **86** 779
[2] Basov D N, Averitt R D and Hsieh D 2017 *Nat. Mat.* **16** 1077
[3] Eckardt A 2017 *Rev. Mod. Phys.* **89** 011004
[4] Goldman N, Budich J C and Zoller P 2016 *Nat. Phys.* **12** 639
[5] Dotti P, Bai Y, Shimasaki T, Dardia A R and Weld D M 2025 *Phys. Rev. Res.* **7** L022026
[6] Wang Y H, Steinberg H, Jarillo-Herrero P and Gedik N 2013 *Science* **342** 453
[7] Mahmood F, Chan C K, Alpichshev Z, Gardner D, Lee Y, Lee P A and Gedik N 2016 *Nat. Phys.* **12** 306
[8] McIver J W, Schulte B, Stein F U, Matsuyama T, Jotzu G, Meier G and Cavalleri A 2020 *Nat. Phys.* **16** 38
[9] Aeschlimann S *et al* 2021 *Nano Lett.* **21** 5028
[10] Reimann J *et al* 2018 *Nature* **562** 396
[11] Ito S *et al* 2023 *Nature* **616** 696
[12] Reimann J, Sumida K, Kakoki M, Kokh K A, Tereshchenko O E, Kimura A, Güdde J and Höfer U 2023 *Sci. Rep.* **13** 5796
[13] Lesko D M B Weitz T Wittigschlager S Li W Heide C Neufeld O and Hommelhoff P arXiv:2407.17917
[14] Merboldt M *et al* 2025 *Nat. Phys.* (https://doi.org/10.1038/s4156 7-025-02889-7)
[15] Choi D, Mogi M, De Giovannini U, Azoury D, Lv B, Su Y, Hübener H, Rubio A and Gedik N 2025 *Nat. Phys.* (https://doi.org/10.1038/s41567-025-02888-8)
[16] Broers L and Mathey L 2021 *Commun. Phys.* **4** 248
[17] Oka T and Kitamura S 2019 *Annu. Rev. Condens. Matter Phys.* **10** 387
[18] Lindner N H, Refael G and Galitski V 2011 *Nat. Phys.* **7** 490
[19] Bao C, Tang P, Sun D and Zhou S 2022 *Nat. Rev. Phys.* **4** 33
[20] Cao H, Sun J T and Meng S 2024 *npj Quantum Mater.* **9** 2397
[21] Schüler M and Beaulieu S 2022 *Commun. Phys.* **5** 164

[22] Fragkos S, Fabre B, Tkach O, Petit S, Descamps D, Schönhense G, Mairesse Y, Schüler M and Beaulieu S 2024 Floquet-Bloch valleytronics (arXiv:2412.03935)
[23] Oka T and Aoki H 2009 *Phys. Rev. B* **79** 081406
[24] Zhou S *et al* 2023 *Nature* **614** 75
[25] Sie E J, McIver J W, Lee Y H, Fu L, Kong J and Gedik N 2015 *Nat. Mater.* **14** 290
[26] Kobayashi Y, Heide C, Johnson A C, Tiwari V, Liu F, Reis D A, Heinz T F and Ghimire S 2023 *Nat. Phys.* **19** 17
[27] Habibovic D, Hamilton K R, Neufeld O and Rego L 2024 *Nat. Rev. Phys.* **6** 663
[28] Jiménez-Galán A, Silva R E F, Smirnova O and Ivanov M 2020 *Nat. Photon.* **14** 728
[29] Neufeld O, Mao W, Hübener H, Tancogne-Dejean N, Sato S A, De Giovannini U and Rubio A 2022 *Phys. Rev. Res.* **4** 033101
[30] Trevisan T V, Villar Arribi P, Heinonen O, Slager R J and Orth P P 2022 *Phys. Rev. Lett.* **128** 066602
[31] Wang Y, Walter A S, Jotzu G and Viebahn K 2023 *Phys. Rev. A* **107** 043309
[32] Neufeld O and Hübener H De Giovannini U and Rubio A 2024 *J. Phys.: Condens. Matter.* **36** 225401
[33] Bhattacharya U, Chaudhary S, Grass T, Johnson A S, Wall S and Lewnstein M 2022 *Phys. Rev. B* **105** L081406
[34] Mitra S, Jiménez-Galán Alvaro, Aulich M, Neuhaus M, Rui E F S Pervak V, Matthias F K and Biswas S 2024 *Nature* **628** 752
[35] Schüler M and Sentef M A 2021 *J. Electron Spectrosc. Relat. Phenom.* **253** 147121
[36] Peskin U and Moiseyev N 1993 *J. Chem. Phys.* **99** 4590
[37] Grifoni M and Hänggi P 1998 *Phys. Rep* **304** 229
[38] Drese K and Holthaus M 1999 *Eur. Phys. J. D* **5** 119
[39] Holthaus M 2015 *J. Phys. B* **49** 013001
[40] Ikeda T N, Tanaka S and Kayanuma Y 2022 *Phys. Rev. Res.* **4** 033075
[41] Baba Y, Junk V, Hogger W, Domínguez-Adame F, Molina R A and Richter K 2024 Radiation-induced dynamical formation of Floquet-Bloch bands in Dirac Hamiltonians (arXiv:2409.00285)
[42] Lebègue S and Eriksson O 2009 *Phys. Rev. B* **79** 115409
[43] Zhu Z Y, Cheng Y C and Schwingenschlögl U 2011 *Phys. Rev. B* **84** 153402
[44] Xiao D, Liu G B, Feng W, Xu X and Yao W 2012 *Phys. Rev. Lett.* **108** 196802
[45] Cao T *et al* 2012 *Nat. Commun.* **3** 887
[46] Yao W, Xiao D and Niu Q 2008 *Phys. Rev. B* **77** 235406
[47] Liu G B, Xiao D, Yao Y, Xu X and Yao W 2015 *Chem. Soc. Rev.* **44** 2643
[48] Papadopoulos N, Watanabe K, Taniguchi T, van der Zant H S J and Steele G A 2019 *Phys. Rev. B* **99** 115414
[49] Baba Y and Gómez A S Floquet $t - t'$ formalism solver in Python for TMDs (available at: https://github.com/yurikobd/Floquet_TMD_ttp)